ACS APPLIED NANO MATERIALS

www.acsanm.org Article

Stable and Monodisperse Iron Nitride Nanoparticle Suspension for Magnetic Diagnosis and Treatment: Development of Synthesis and Surface Functionalization Strategies

Kai Wu,*[,§] Jinming Liu,[§] Renata Saha, Bin Ma, Diqing Su, Vinit Kumar Chugh, and Jian-Ping Wang*

Cite This: *ACS Appl. Nano Mater.* 2021, 4, 4409−4418 Read Online

ACCESS | Metrics & More | Article Recommendations | Supporting Information

ABSTRACT: The past decade has seen tremendous progress in the synthesis and surface functionalization of iron oxide nanoparticles (IONPs) for a variety of biomedical applications. However, there is still a growing demand on magnetic nanoparticles with higher magnetic moments for more sensitive diagnosis and lower dose treatments in magnetic bioassays, imaging, and therapies. In view of this need, the γ'-Fe_4N nanoparticle, with around 3 times higher saturation magnetizations than IONPs, becomes one promising alternative for these applications. However, the large and non-uniformly distributed sizes of γ'-Fe_4N nanoparticles hinder the biomedical applications. These synthesized γ'-Fe_4N nanoparticles are not suitable for biomedical applications at the current stage. Herein, we have developed and demonstrated a wet ball milling method along with different surface-active media to produce ultrastable, monodispersed, uniformly sized, and sub-100 nm γ'-Fe_4N nanoparticles in solvents. Different standard characterization methods such as transmission electron microscopy, nanoparticle tracking analysis, and Fourier-transform infrared spectroscopy are carried out to measure the physicochemical properties of these surface-functionalized γ'-Fe_4N nanoparticles. It is confirmed that the functional chemical groups have been successfully anchored on our purified sub-100 nm γ'-Fe_4N nanoparticles, which allows for convenient subsequent conjugation of proteins, nucleic acids, and drugs for future *in vitro* and *in vivo* biomedical applications.

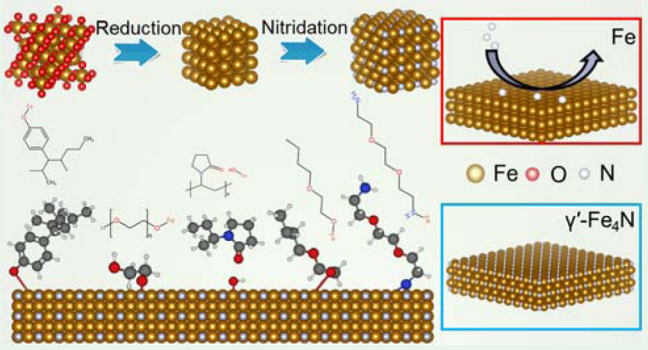

KEYWORDS: *iron nitride, surface functionalization, surface-active media, colloidal stability, monodispersed*

1. INTRODUCTION

In recent years, iron oxide nanoparticles (IONPs) have been widely used for magnetic diagnosis and treatment such as magnetic resonance imaging, magnetic particle imaging, gene/drug delivery, magnetic hyperthermia therapy, magnetic separation, and magnetic biosensors.[1−14] The research interest in pursuing inexpensive, high magnetic moment, low biotoxicity, colloidal stable, and environmentally friendly magnetic nanoparticles (MNPs) is growing rapidly in view of the increasing demands of high sensitivity magnetic diagnosis and low dose treatments.[12,15−19] To this end, γ'-Fe_4N becomes one promising candidate because (1) both iron and nitrogen are inexpensive, have low biotoxicity, and are environment-friendly and (2) the saturation magnetization of γ'-Fe_4N is around 3 times higher than that of IONPs.[20,21]

However, the preparation of colloidal stable, uniformly sized, and sub-100 nm γ'-Fe_4N nanoparticles for biomedical applications is still challenging at the current stage. Nowadays, the gas nitriding method is widely used for mass production of γ'-Fe_4N nanoparticles.[20,22,23] In this route, IONPs are usually used as the precursor and then a hydrogen reduction step is carried out to remove oxygen and get reduced Fe nanoparticles. After that, a mixture of ammonia and hydrogen gas is used for nitriding at a temperature around 400−600 °C. Single-phase γ'-Fe_4N nanoparticles have been reported using this method.[20] Although the gas nitriding approach can realize massive production of high-magnetic-moment γ'-Fe_4N nanoparticles due to the relatively high processing temperature, some nanoparticles are sintered together, leading to a larger and wider size distribution. On the other hand, nanoparticles that are sub-100 nm and with a narrow size distribution are required for most biomedical applications.[11,12,24−28] Although there have been many literature studies reporting the stabilization of INOPs with different functional groups under various solution conditions,[29−33] the direct surface chemical modification of γ'-Fe_4N nanoparticles has never been reported.

Received: December 22, 2020
Accepted: April 13, 2021
Published: April 23, 2021

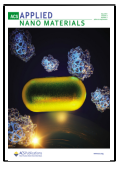

https://doi.org/10.1021/acsanm.0c03421
ACS Appl. Nano Mater. 2021, 4, 4409−4418

Herein, we developed a synthesis and surface functionalization strategy to obtain ultrastable, monodispersed, sub-100 nm, narrow-size-distributed γ'-Fe_4N nanoparticle colloidal suspensions.

In this paper, we first synthesized γ'-Fe_4N nanoparticles through a gas nitriding approach. Then, these γ'-Fe_4N nanoparticles are surface-functionalized by wet ball milling along with four different surface-active media: water (as a negative control group), a commercial nanoparticle surfactant, oleic acid (OA), and tetramethylammonium hydroxide solution (TMAOH), followed by different centrifugation processes to collect the uniformly sized, sub-100 nm γ'-Fe_4N nanoparticles from the supernatants. The morphologies and hydrodynamic sizes of processed γ'-Fe_4N nanoparticles as well as the surface chemical groups on nanoparticles are characterized by the standard transmission electron microscopy (TEM), nanoparticle tracking analysis (NTA), and Fourier-transform infrared spectroscopy (FTIR). The colloidal stability of processed γ'-Fe_4N nanoparticle suspensions is evaluated using a zeta potential analyzer (ZPA) and through a 21-day period observation period.

2. EXPERIMENTAL SECTION

2.1. Materials. The γ-Fe_2O_3 nanoparticle powder is purchased from MTI Corporation. The commercial nanoparticle surfactant (in water dispersion) is purchased from US Research Nanomaterials, Inc. This surfactant product is a mixture of following substances: nonylphenol ($C_{15}H_{24}O$, CAS#: 25154-52-3), a polyoxyalkylene amine derivative (CAS#: 68511-96-6), polyethylene glycol [$C_{14}H_{22}O$-$(C_2H_4O)_n$, n = 9−10, CAS#: 9002-93-1], polyvinylpyrrolidone ($(C_6H_9NO)_n$, CAS#: 9003-39-8), butyl ethanoate ($C_6H_{12}O_2$, CAS#: 123-86-4), and ethylene glycol monobutyl ether ($C_6H_{14}O_2$, CAS#: 111-76-2). OA ($C_{18}H_{34}O_2$, CAS#: 112-80-1) is purchased from Thermo Fisher Scientific. TMAOH [$N(CH_3)_4OH$, CAS#: 75-59-225, wt % in water] is purchased from Sigma-Aldrich.

2.2. Synthesis of γ'-Fe_4N Nanoparticles. γ-Fe_2O_3 nanoparticles (~20 nm) are used to prepare γ'-Fe_4N by a gas nitriding approach. The precursor (γ-Fe_2O_3 nanoparticles) is put in a tube furnace with a diameter of 1 inch, as shown in Figure 1a. Once the 100 sccm H_2 gas is introduced, the furnace temperature is increased from room temperature to 350−450 °C at a rate of ~10 °C/min. The precursor is reduced in hydrogen for 2−5 h to obtain Fe nanoparticles. This process is marked as the reduction step in Figure 1b. After that, the temperature is kept at 400 °C, and ammonia of 60 sccm (or 40 sccm) and hydrogen of 20 sccm (or 40 sccm) are introduced into the tube furnace for nitriding (Figure 1b).

The nitriding time is in the range of 2−3 h. Active nitrogen reacts with the reduced Fe to form γ'-Fe_4N, which is shown in the schematic drawing in Figure 1c. After the nitriding process, the furnace is cooled down to 50 °C, and then, the γ'-Fe_4N nanoparticles are directly transferred to a glovebox under a nitrogen atmosphere. The samples for vibrating sample magnetometry and X-ray diffraction (XRD) are also prepared in the glovebox to avoid further oxidation.

2.3. γ'-Fe_4N Nanoparticle Surface Modification. Herein, four γ'-Fe_4N nanoparticle suspensions are prepared through the wet ball milling and centrifugation processes and then washed out by a magnetic separation step, as shown in Figure 2. To begin with, in each sample, 50 mg of γ'-Fe_4N nanoparticle powder is first dispersed in 5 mL of water (labeled as sample A), 5 mL of 5 vol/vol % commercial nanoparticle surfactant in water (labeled as sample B), 5 mL of 25 vol/vol % OA in ethanol (labeled as sample C), and 5 mL of 25 wt % tetramethylammonium hydroxide (TMAOH) in water (labeled as sample D), as shown in Figure 2a. Then, each sample is wet-ball-milled at 350 rpm for 4 h with a time interval of 30 min, as shown in Figure 2b. It should be noted that as far as the authors are aware, there are no reports on surface modification of iron nitride nanoparticles (e.g., Fe_xN, α''-$Fe_{16}N_xZ_{2-x}$, and α'-$Fe_8N_xZ_{1-x}$, where Z includes at least one of C, B, or O). Thus, the authors choose the surface-active media based on the literature studies reporting the surface modification of IONPs.[34−42]

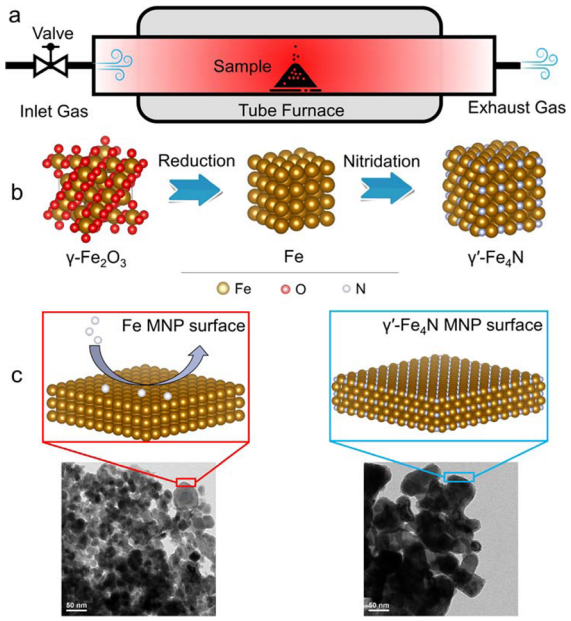

Figure 1. (a) Schematic view of the γ'-Fe_4N nanoparticle synthesis process by a gas nitriding approach. (b) Space-filling models of γ-Fe_2O_3, Fe, and γ'-Fe_4N crystal structure transitions from reduction and nitridation steps. (c) Space-filling models of nitrogen atoms on the surface of the Fe nanoparticle. Nitrogen atoms diffuse into reduced Fe nanoparticles to form γ'-Fe_4N. Insets are the TEM images of Fe and γ'-Fe_4N nanoparticles.

Despite the high yield in the synthesis of γ'-Fe_4N nanoparticles by means of the gas nitriding approach, due the high temperatures in the gas nitriding process, the sintered nanoparticles of large sizes are not favored for biomedical applications. Thus, a centrifugation step is carried out to maintain the sub-100 nm γ'-Fe_4N nanoparticles and discard larger nanoparticles. There is a trade-off between obtaining the uniformly sized, sub-100 nm nanoparticles and reducing the loss rate of raw materials (i.e., the nanoparticle powder after the wet ball milling step). Herein, we explored two centrifugal speeds, 2 krpm and 11 krpm. Among them, more nanoparticles can be retained, and the size distribution may be wider if the sample is centrifuged at 2 krpm. On the other hand, centrifugation at 11 krpm can get a narrower size distribution, but the number of nanoparticles is lower.

After the wet ball milling process, the turbid suspensions are allotted into three 1.5 mL vials. The first vial is centrifuged at 2 krpm for 30 min, and 500 μL of the supernatant is drawn from this vial. The surface-functionalized γ'-Fe_4N nanoparticles from each supernatant are separated using a permanent magnet, then washed three times by either water (for nanoparticles from samples A, B, and D) or ethanol (for nanoparticles from sample C), and finally re-dispersed in water or the ethanol solvent to the desired volumes for different characterization purposes. These γ'-Fe_4N nanoparticle suspensions are labeled as X@2k (X = A, B, C, and D), as shown in Figure 2c.

Similarly, the second vial is centrifuged at 11 krpm for 30 min, and 500 μL of the supernatant is drawn from this vial. After magnetic separation and washout three times and re-dispersion in water or the ethanol solvent, these γ'-Fe_4N nanoparticle suspensions are labeled as X@11k (X = A, B, C, and D), as shown in Figure 2d. The remaining wet cakes from the bottoms of these vials are magnetically separated, washed three times, dried in a N_2 glovebox at room temperature, and labeled as X@pellet (X = A, B, C, and D) for further characterizations.

The third vial is centrifuged at 2 krpm for 30 min, and 1 mL of the supernatant is drawn from this vial. These supernatants are labeled as X@supernatant (X = A, B, C, and D) and sealed in transparent glass

https://doi.org/10.1021/acsanm.0c03421
ACS Appl. Nano Mater. 2021, 4, 4409−4418

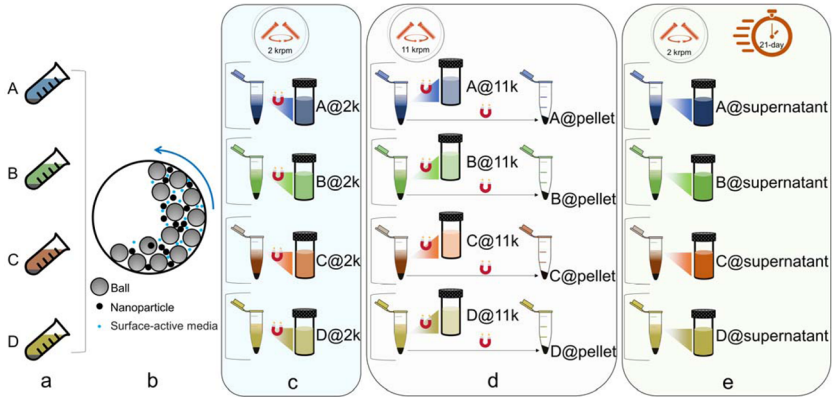

Figure 2. Schematic view of γ'-Fe_4N nanoparticle surface modification steps. (a) 50 mg of γ'-Fe_4N nanoparticle powder is dispersed in different surface-active media before the (b) wet ball milling step. (c) The collected and allotted turbid suspensions are centrifugated at 2 krpm for 30 min. Then, the supernatants are extracted, washed out, re-dispersed in solvents, and labeled as X@2k (X = A, B, C, and D). (d) Samples X@11k (X = A, B, C, and D) are prepared in the same manner as X@2k except that the centrifugation speed is set at 11 krpm. The wet cakes from these vails are extracted and labeled as X@pellet (X = A, B, C, and D). (e) The allotted turbid suspensions are centrifuged at 2 krpm for 30 min, and 1 mL of supernatants is drawn for 21-day colloidal stability observation. The magnet symbol indicates three cycles of magnetic separation, and wash steps are carried out when preparing the samples. Photographs of these aforementioned γ'-Fe_4N nanoparticle suspensions are provided and can be found from the Supporting Information, S1.

bottles for a 21-day colloidal stability observation, as shown in Figure 2e.

2.4. Magnetic Property Characterization. The nanoparticle samples, γ-Fe_2O_3 and γ'-Fe_4N, are stored in the N_2 glovebox to avoid oxidations. All the nanoparticle samples for magnetic characterization are prepared in the glovebox. Certain amounts of nanoparticles are weighted and sealed in parafilms to prevent further oxidation after samples are taken out of the glovebox. Hysteresis loops are measured using a physical properties measurement system (PPMS, Quantum Design Inc.) to obtain the magnetic properties of these nanoparticles such as the saturation (M_s) and coercivity (H_c).

2.5. Crystal Structure Characterization. γ-Fe_2O_3 and γ'-Fe_4N nanoparticle samples for XRD patterns are also prepared in the glovebox. Certain amounts of nanoparticles are put on a piece of the glass substrate, and the epoxy is used to seal the nanoparticles to prevent oxidation after the samples are taken out of the glovebox. When the epoxy becomes dry and solid, these samples are used for the XRD measurements. The XRD patterns are characterized using a Bruker D8 Discover 2D equipped with a Co radiation source operated at 45 kV and 40 mA. For a convenient comparison, we converted the XRD patterns into a Cu radiation source using MDI Jade software.

2.6. Nanoparticle Morphology and Size Characterization. The morphologies of γ'-Fe_4N nanoparticle cores are characterized by TEM (FEI Tecnai T12). Briefly, 10 μL of X@2k and X@11k (X = A, B, C, and D) nanoparticle colloidal suspensions is dropped on TEM grids and air-dried at room temperature before TEM imaging.

The hydrodynamic sizes of these surface-functionalized γ'-Fe_4N nanoparticles are measured by NTA (Nanosight LM-10). Briefly, 1.5 mL of samples X@2k and X@11k (X = A, B, C and D) is used for the hydrodynamic size measurements on the nanoparticle tracking analyzer. The nanoparticle tracking analyzer uses a 400 nm (near UV) laser to track the motion of γ'-Fe_4N nanoparticles suspended in solvents (i.e., water for samples A, B, and D and ethanol for sample C) and then calculates the size distributions for nanoparticles between 10 nm and 1 μm.

2.7. Nanoparticle Surface Chemical Group Characterization. The chemical groups functionalized on γ'-Fe_4N nanoparticle surfaces are characterized using an FTIR spectrometer (FTIR, Thermo Scientific Nicolet iS50 FTIR) on the main detector MCT-A (7000−600 cm^{-1}), with a KBr beam splitter and a resolution of 2 cm^{-1}. A total of 32 scans are taken on each sample. Samples X@pellet (X = A, B, C, and D) are evenly spread and dried on a barium fluoride (BaF_2) window (diameter 25.4 mm, thickness 2 mm, purchased from EKSMA Optics, UAB) for FTIR transmittance spectrum recording. In addition, the FTIR transmittance spectra of the commercial surfactant product, OA, and TMAOH are also recorded for direct comparisons. These liquid samples are sealed between two BaF_2 windows before FTIR characterizations.

2.8. Zeta Potential of Nanoparticles. A ZPA (Stabino) is used to measure the particle charge distribution or the zeta potential of the surface-functionalized γ'-Fe_4N nanoparticles from solvents (water or ethanol). Briefly, 5 mL of samples X@2k (X = A, B, C, and D) is prepared and sonicated for 30 min before the zeta potential measurements.

3. RESULTS AND DISCUSSION

3.1. Magnetic Properties of Synthesized γ'-Fe_4N Nanoparticles. The static magnetic hysteresis loops of γ-Fe_2O_3 (the precursor) and the synthesized γ'-Fe_4N nanoparticles are shown in Figure 3a,b. From Figure 3a, the magnetizations of γ-Fe_2O_3 and γ'-Fe_4N nanoparticles saturate at around 2.5 and 7 kOe, respectively. The calculated specific saturation magnetizations (M_s) of γ-Fe_2O_3 and synthesized γ'-Fe_4N nanoparticles at 15 kOe are 57.7 and 182.7 emu/g, respectively. Figure 3b is an enlarged view of the hysteresis loops within a magnetic field of ±2 kOe. The coercivities (H_c) of γ-Fe_2O_3 and synthesized γ'-Fe_4N nanoparticles are 0 and 310 Oe, respectively. Since some γ'-Fe_4N nanoparticles are sintered during the high-temperature gas nitriding process, these sintered nanoparticles are larger in size and thus unlikely to be superparamagnetic. As a result, the synthesized γ'-Fe_4N nanoparticles show ferromagnetic properties with large magnetic coercivity and remanence, as seen in Figure 3a. On the other hand, the γ-Fe_2O_3 (the precursor) shows superparamagnetic properties with zero magnetic coercivity and remanence. The specific magnetizations (M) of both nanoparticles under different magnetic fields, coercivities (H_c), remanence magnetizations (M_r), and magnetic susceptibilities (χ) are summarized in Table 1. The high H_c and large remanence of γ'-Fe_4N are caused by the sintering during the high-temperature gas nitriding process. These sintered γ'-Fe_4N particles with wider size distributions and larger sizes (as shown in Figures 4 and 5a) are not suitable for most biomedical applications. Thus, the goal of this work is to break these larger sintered particles, separate smaller nanoparticles by a wet ball milling method with surface-active media, and then

https://doi.org/10.1021/acsanm.0c03421
ACS Appl. Nano Mater. 2021, 4, 4409−4418

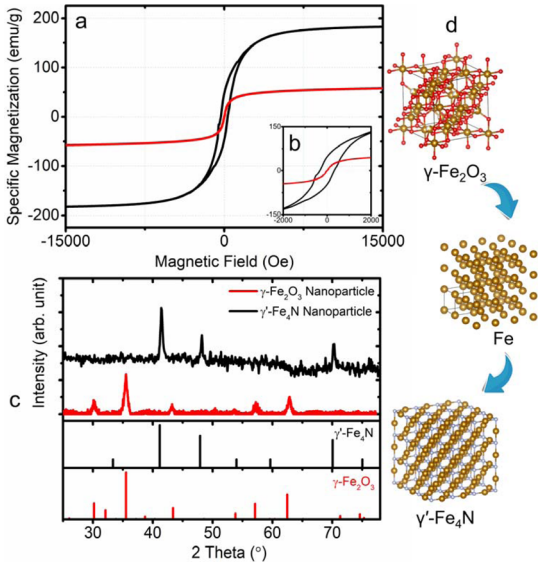

Figure 3. (a) Static magnetic hysteresis loops of γ-Fe_2O_3 and the synthesized γ'-Fe_4N nanoparticles measured by PPMS with the external magnetic field swept from −15 to +15 kOe. The inset figure (b) shows hysteresis loops within a field range of ±2 kOe. (c) XRD patterns of γ-Fe_2O_3 and the synthesized γ'-Fe_4N nanoparticles. (d) Ball-and-stick models of γ-Fe_2O_3, Fe, and γ'-Fe_4N showing the crystal structure change that causes hysteresis loops and XRD pattern differences.

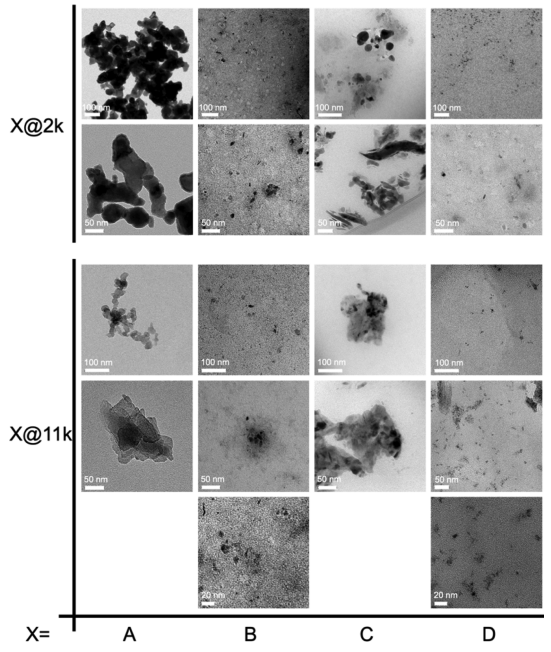

Figure 4. TEM images of X@2k and X@11k samples (X = A, B, C, and D) under different scale bars. Samples A and C show severe aggregations of γ'-Fe_4N nanoparticles, while samples B and D show monodispersed nanoparticles even after the centrifugation at 2 krpm for 30 min. The magnetic core size distributions of γ'-Fe_4N nanoparticles from samples X@11k are obtained from TEM images and provided in the Supporting Information, S2.

centrifuge to extract and purify monodispersed, uniformly sized, and sub-100 nm γ'-Fe_4N nanoparticles.

The XRD patterns of the precursor γ-Fe_2O_3 and synthesized γ'-Fe_4N nanoparticles are shown in Figure 3c. The powder diffraction files (PDFs) of these two materials are also plotted at the bottom panels of the XRD patterns. The XRD pattern of starting IONPs matches well with the PDF, indicating that the starting materials are γ-Fe_2O_3. These IONPs are then reduced by hydrogen gas to get rid of oxygen and create preferable microstructures for the following nitriding process.[43−46] After nitriding, the XRD patterns show that the main phase is γ'-Fe_4N. Thus, γ'-Fe_4N nanoparticles are successfully synthesized by the gas nitriding approach. The ball-and-stick models of γ-Fe_2O_3 and γ'-Fe_4N are shown in Figure 3d to provide a brief view of how the crystal structure changes from γ-Fe_2O_3 to reduced Fe and synthesized γ'-Fe_4N.

3.2. Morphologies of Surface-Functionalized γ'-Fe_4N Nanoparticles. The morphologies of surface-functionalized γ'-Fe_4N nanoparticles by different surface-active media are imaged by TEM. It should be noted that this morphology imaging is used to observe the magnetic cores of synthesized γ'-Fe_4N nanoparticles, and thus, the sizes read from TEM images are different from the hydrodynamic sizes read from NTA.

The TEM images of samples X@2k and X@11k (X = A, B, C, and D) are given under different scale bars, as shown in Figure 4. It can be clearly seen that γ'-Fe_4N nanoparticles that are wet-ball-milled in water (samples A@2k and A@11k) and

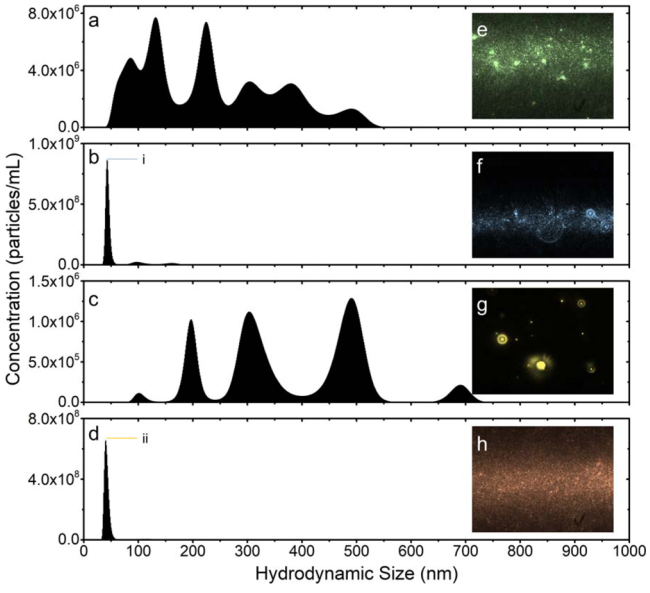

Figure 5. (a−d) Hydrodynamic size distributions of X@2k samples, X = A, B, C, and D, respectively, measured by NTA. (e−h) NTA photos of γ'-Fe_4N nanoparticles, respectively. (i,ii) Peaks at 44 and 41 nm, respectively.

Table 1. Magnetic Property Comparisons on γ-Fe_2O_3 and the Synthesized γ'-Fe_4N Nanoparticles

	M_s (15 kOe)	M (5 kOe)	M (1 kOe)	H_c	M_r	χ (±1 kOe)
γ-Fe_2O_3	57.7 emu/g	51.3 emu/g	38.0 emu/g	0 Oe	0 emu/g	0.038 emu/g/Oe
γ'-Fe_4N	182.7 emu/g	168.0 emu/g	106.3 emu/g	310 Oe	45 emu/g	0.093 emu/g/Oe

https://doi.org/10.1021/acsanm.0c03421
ACS Appl. Nano Mater. 2021, 4, 4409−4418

in OA (samples C@2k and C@11k) form large clusters. This indicates that (1) wet ball milling in water and OA cannot effectively separate γ'-Fe_4N nanoparticles; (2) these γ'-Fe_4N nanoparticles are not superparamagnetic and thus form clusters due to non-zero remanence; (3) these γ'-Fe_4N nanoparticles processed with water and OA would not be colloidally stable and may form sediments in solvents.

On the other hand, the γ'-Fe_4N nanoparticles that are wet-ball-milled in the commercial surfactant product and TMAOH are monodispersed. Samples B@2k, B@11k, D@2k, and D@11k show monodispersed and small-size γ'-Fe_4N nanoparticles. This indicates that (1) centrifuging at 2krpm for 30 min is good enough to extract uniform-sized, monodispersed, and sub-100 nm γ'-Fe_4N nanoparticles; (2) these nanoparticles do not form clusters and thus will be colloidally stable. Furthermore, many γ'-Fe_4N nanoparticles with sizes below 20 nm are observed, while the theoretical size limit for γ'-Fe_4N nanoparticles to be superparamagnetic is 19 nm.[47,48]

NTA is used to measure the hydrodynamic size of the γ'-Fe_4N nanoparticles after different surface modification processes. A statistical average of five independent NTA measurements are carried out on samples X@2k (X = A, B, C, and D). During each NTA measurement, a 1 min video of the γ'-Fe_4N nanoparticles is recorded under the microscope, and snapshots of the respective samples are given in Figure 5e–h. From Figure 5a,c,e,g, it is evident that the γ'-Fe_4N nanoparticles from samples A@2k and C@2k are severely clustered, with prominent peaks at the greater side of the hydrodynamic size. The significant clustering of the nanoparticles is also seen from the TEM images in Figure 4 for samples A@2k and C@2k. However, from Figure 5b,d,f,h, it is evident that the samples B@2k and D@2k show prominent peaks at hydrodynamic sizes of 44 and 41 nm, respectively. This is also supported by the TEM images in Figure 4. Although the scale bars in TEM images of Figure 4 show that some particles are of the order of 20 nm in size, the hydrodynamic size measurements show that sample B@2k mostly has a size of 44 nm and sample D@2k mostly has a size of 41 nm due to the fact that the surfactant coatings of nanoparticles sum up to the size. On the contrary, TEM only captures the core size of the nanoparticles. Table 2 shows the 10th, 50th, and 90th

Table 2. Percentile and Average Sizes of γ'-Fe_4N Nanoparticles in X@2k Samples (X = A, B, C, and D)

X@2k	A (nm)	B (nm)	C (nm)	D (nm)
10th	86.8	39.7	198.1	37.8
50th	220.8	44.4	352.3	41.5
90th	405.3	102.8	514.7	49.8
average size	233.8	58.5	382.1	45.3

percentiles as well as the mean hydrodynamic sizes of γ'-Fe_4N nanoparticles from samples X@2k (X = A, B, C and D) as obtained from the NTA measurements. The hydrodynamic size distributions and percentile size distributions of samples X@11k (X = A, B, C, and D) are provided in Supporting Information, S3.

3.3. Colloidal Stability of γ'-Fe_4N Nanoparticles. The colloidal stabilities of surface-functionalized γ'-Fe_4N nanoparticles by different surface-active media are appraised through a 21-day period observation on samples X@supernatant (X = A, B, C, and D). As shown in Figure 6a, no observable sedimentations are present in any of these samples.

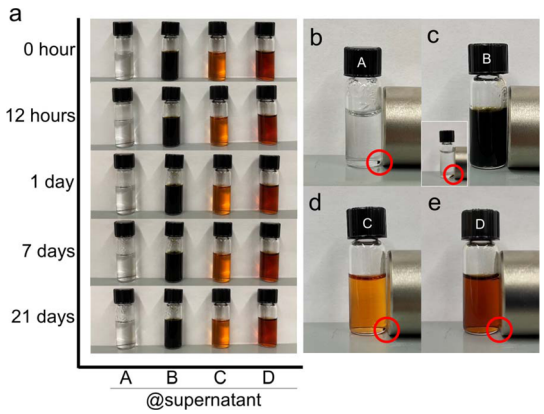

Figure 6. Colloidal stability observation of X@supernatant (X = A, B, C, and D) over a 21-day period of observation. (a) Photographs of X@supernatant (X = A, B, C, and D) γ'-Fe_4N nanoparticle colloidal suspensions from day 0 to day 21. (b–e) Photographs of γ'-Fe_4N nanoparticles separated using a permanent magnet from samples A–D@supernatant, respectively.

However, these types of observations by bare eyes are not very reliable due to the low amount of γ'-Fe_4N nanoparticles presenting in the suspensions. Figure 6b–e shows the magnetically separated γ'-Fe_4N nanoparticle wet cakes using a permanent magnet, proving that there are a small number of nanoparticles in each X@supernatant sample. It should be noted that due to the dark background color of the solvent in sample B@supernatant, a second photo of the separated nanoparticles (wet cake) is given in the inset of Figure 6c after three times of magnetic washout with water.

In addition, the colloidal stabilities of X@2k (X = A, B, C, and D) samples are further proved by the zeta potentials. In brief, the zeta potentials of surface-functionalized γ'-Fe_4N nanoparticles in the solvent are −29.13, −26.27, −0.55, and −29.99 mV, respectively, for A, B, C, and D. This indicates that γ'-Fe_4N nanoparticles processed by commercial surfactants, water, and TMAOH are relatively stable due to a large electrokinetic potential (or electrostatic repulsion), while, on the other hand, γ'-Fe_4N nanoparticles treated by OA will rapidly coagulate.

Although zeta potential results indicate that γ'-Fe_4N nanoparticles treated by commercial surfactants, water, and TMAOH should be colloidal stable and that treated by OA should not, the TEM images and NTA results show that only the γ'-Fe_4N nanoparticles that are treated by commercial surfactants and TMAOH are uniformly sized and monodispersed, while nanoparticles treated by water are not. This is due to the fact that although γ'-Fe_4N nanoparticles treated by water show a large electrokinetic potential (or electrostatic repulsion), there are no surface chemical groups functionalized on these nanoparticles, and the non-zero remanences of these nanoparticles are the cause of clustering.

3.4. Chemical Groups on γ'-Fe_4N Nanoparticle Surfaces. The surface chemical groups of γ'-Fe_4N nanoparticles from X@pellet samples (X = A, B, C, and D) are characterized by FTIR. The IR transmittance spectra are given in Figure 7. For comparison, the transmittance spectra of original surface-active media (the commercial surfactant for sample B, OA for sample C, and TMAOH for sample D) are plotted in parallel. The chemical structures of original surface-active media are drawn in parallel with IT transmittance spectra in Figure 7e–g.

https://doi.org/10.1021/acsanm.0c03421
ACS Appl. Nano Mater. 2021, 4, 4409–4418

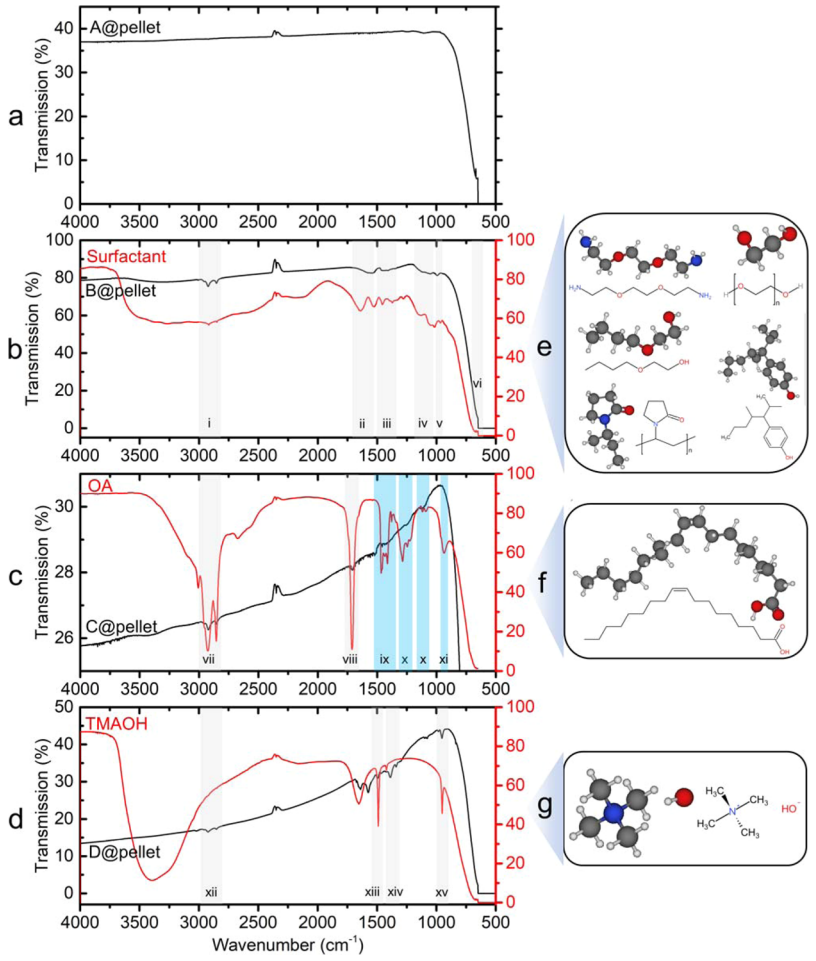

Figure 7. FTIR transmittance spectrum of (a) A@pellet, (b) B@pellet (black curve) and the commercial surfactant product (red curve), (c) C@pellet (black curve) and OA solution (red curve), and (d) D@pellet (black curve) and TMAOH solution (red curve). The gray regions indicate that the characteristic transmittance peaks are observed from both X@pellet and its original surface-active media. The blue regions indicate that the characteristic transmittance peaks from original surface-active media are absent from the C@pellet sample. (e–g) Chemical compounds in the commercial surfactant product, OA, and TMAOH, respectively. The transmittance peaks and the corresponding chemical groups are summarized in Table 3.

The FTIR transmittance spectrum of A@pellet in Figure 7a does not show any remarkable peaks, and thus, γ'-Fe_4N nanoparticles are not functionalized with any chemical groups through the wet ball milling process in water. It is worth to mention that once the γ'-Fe_4N nanoparticles are brought out of the vacuum chamber, there is a mixed mode layer of the hydroxyl group and water formed on the nanoparticle surface.[49,50] This causes some weak spikes around 3600 and 1600 cm^{-1}. Usually, these peaks from water are removed by dehumidifying or pumping the FTIR chamber, subtracted as the background spectrum (without the sample loaded, only the BaF_2 window loaded), and averaged by carrying out 32 FTIR scans. However, from sample C@pellet, as shown in Figure 7c, some visible peaks caused by this mixed mode layer of the hydroxyl group and water are still present. It does not affect the analysis of FTIR results. On the other hand, this mixed mode layer of the hydroxyl group and water facilitates the subsequent nanoparticle surface modifications. Figure 8 shows the schematic views of these chemical groups bonding to the Fe atoms through the hydroxyl groups on the surface of γ'-Fe_4N nanoparticles. The hydroxyl group on the surface of the nanoparticles tends to bond with the chemical groups with high electron affinity. The grain size and chemical structures of the final product can be engineered by optimizing the type and concentration of the surfactants.

While in Figure 7b, the chemical groups such as the benzene derivative (~700 cm^{-1}, marked as vi in Figure 7b) and C═C bending (960–1000 cm^{-1}, marked as v in Figure 7b) are from nonylphenol, C–N and C–O stretching (1000–1300 cm^{-1}, marked as vi in Figure 7b) come from nonylphenol, the polyoxyalkelene amine derivative, polyethylene glycol, polyvinylpyrrolidone, and ethylene glycol monobutyl ether. Other chemical groups and the corresponding FTIR transmittance peaks are listed in Table 3. It is confirmed that the surface-active groups from this commercial surfactant product are successfully functionalized on γ'-Fe_4N nanoparticles after the wet ball milling process. Figure 8a gives the schematic views of these chemicals bonds on the γ'-Fe_4N nanoparticle surface through hydroxyl groups.

The transmittance spectrum of C@pellet is shown in Figure 7c; the very weak peaks of C–H stretching (2800–3000 cm^{-1}, marked as vii in Figure 7c) and C═O stretching (~1750 cm^{-1}, marked as viii in Figure 7c) are observed. However, the stronger C–H bending (1400–1500 cm^{-1}, marked as ix in Figure 7b), C–O stretching (~1250 and 1100 cm^{-1}, marked as x in Figure 7c), and the C═C bending peak at 885–995

https://doi.org/10.1021/acsanm.0c03421
ACS Appl. Nano Mater. 2021, 4, 4409–4418

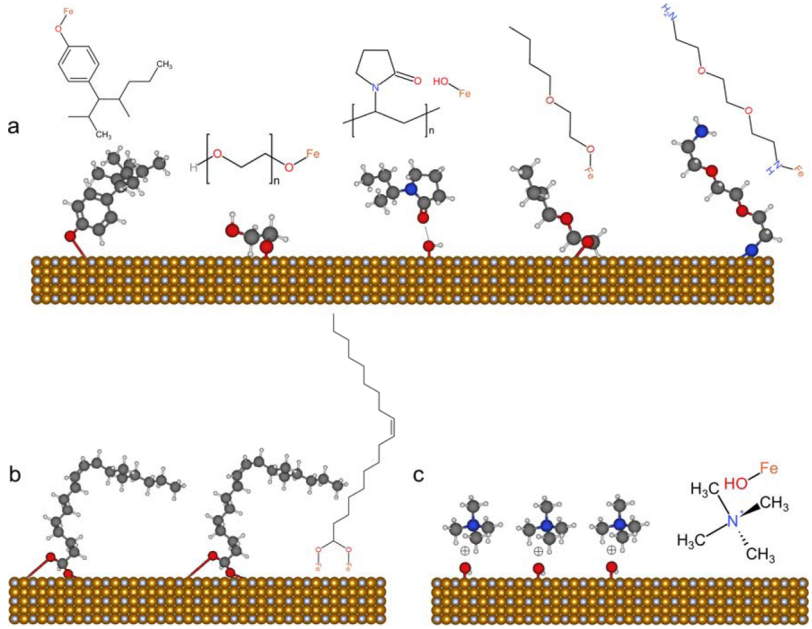

Figure 8. Schematic views of (a) nanoparticle surfactants (nonylphenol, the polyoxyalkylene amine derivative, polyethylene glycol, polyvinylpyrrolidone, butyl ethanoate, and ethylene glycol monobutyl ether). (b) OA and (c) TMAOH chemical groups bonded on the γ'-Fe_4N nanoparticle surface through the hydroxyl group on Fe atoms.

cm^{-1}, marked as xi in Figure 7c, are absent from C@pellet. Thus, OA is not successfully functionalized on γ'-Fe_4N nanoparticles. This also explains why these nanoparticles cluster from TEM images (as shown in Figure 4), showing wide and large size distributions (as shown in Figure 5c) as well as low zeta potentials. Although the OA groups have been reported to be successfully coated on iron oxide nanoparticles by many groups,[35,36,40] unfortunately, only a very less amount of OA groups is bonded on our γ'-Fe_4N nanoparticles. Figure 8b shows the schematic views of the OA bond on the γ'-Fe_4N nanoparticle surface.

The transmittance spectrum of D@pellet is shown in Figure 7d, and the characteristic C−H bending and stretching peaks at 2840−3000 cm^{-1} (marked as xii in Figure 7d), 1380−1450 cm^{-1} (marked as xiii in Figure 7d), and 880 cm^{-1} (marked as xv in Figure 7d) and C−N stretching at ∼1300 cm^{-1} (marked as xiv in Figure 7d) are observed, indicating that TMAOH has been successfully functionalized on γ'-Fe_4N nanoparticles. Figure 8c shows the schematic views of the TMAOH bond on the γ'-Fe_4N nanoparticle surface.

3.5. Crystal Structure of Surface-Functionalized γ'-Fe_4N Nanoparticles. During the wet ball milling process, different surfactants were added, and the milling speed was low (350 rpm). The decomposition temperature of γ'-Fe_4N is above 600 °C based on the Fe−N phase diagram.[51] The surfactants, except water, can also help protect nanoparticles from oxidation during the milling process.[52] Thus, the produced nanoparticles should still conserve the original phase and have similar magnetic properties. To demonstrate that the nanoparticles after wet ball milling with the four surface-active media (A: water, B: 5 vol/vol % commercial nanoparticle surfactant in water, C: 25 vol/vol % OA in ethanol, D: 25 wt % TMAOH in water) are still γ'-Fe_4N, we synthesized a new batch of γ'-Fe_4N nanoparticles as described in Section 2.2, and then, X@pellet samples (X = A, B, C, and D) were prepared as described in Figure 2. The crystal structure characterizations on the newly synthesized γ'-Fe_4N nanoparticle powder and X@pellet samples are shown in Figure 9. The XRD patterns of newly synthesized γ'-Fe_4N nanoparticles and the γ'-Fe_4N peaks are labeled. However, for this batch of samples, we can see the reduced Fe phase due to the insufficient nitriding step from Figure 9a. However, this does not affect our assessment of whether wet ball milling with the four surface-active media will change the crystal structure of nanoparticles. Figure 9b−e shows the XRD patterns of A@pellet, B@pellet, C@pellet, and D@pellet after the wet ball milling process. All the visible Fe_4N (111) and Fe_4N(200) peaks are labeled, as well as the Fe(110) peak (due to the insufficient nitriding step, which is proved from the starting material γ'-Fe_4N powder). It indicates that the wet ball milling step with four surface-active media does not change the crystal structures of the produced nanoparticles. The crystal structure characterizations by XRD are strong pieces of evidence to prove that the produced nanoparticles after the ball milling step are still γ'-Fe_4N.

4. CONCLUSIONS

In this paper, we have successfully surface-functionalized and extracted ultrastable, monodispersed, uniformly sized, and sub-100 nm γ'-Fe_4N nanoparticles. Although the gas nitriding approach could realize the massive production of γ'-Fe_4N nanoparticle powder, the sintering issue caused by the high temperature reduction and nitridation steps brings new challenges to the further usage of high-moment γ'-Fe_4N nanoparticles in biomedical applications such as magnetic diagnosis and treatment. By applying a wet ball milling method along with different surface-active media, the sintered larger γ'-Fe_4N particles are broken and smaller nanoparticles are separated by surface coating of different chemical groups. A follow-up step of centrifugation can effectively extract these sub-100 nm and uniformly sized γ'-Fe_4N nanoparticles from the turbid suspensions. The TEM images indicate that many of these processed γ'-Fe_4N nanoparticles show a magnetic core size of sub-20 nm. Due to the irregular shapes of γ'-Fe_4N

https://doi.org/10.1021/acsanm.0c03421
ACS Appl. Nano Mater. 2021, 4, 4409−4418

Table 3. Chemical Groups Coated on γ'-Fe_4N Nanoparticles

sample index	label	chemical group	sources
B@ pellet	i	C−H stretching	all[a]
	ii	C═O stretching	polyvinylpyrrolidone
		C−O stretching	polyoxyalkylene amine derivative, polyethylene glycol, ethylene glycol monobutyl ether
		N−H bending	polyoxyalkylene amine derivative
	iii	O−H bending	nonylphenol, polyethylene glycol, ethylene glycol monobutyl ether
		C−H bending	all[a]
	iv	C−N stretching	polyoxyalkylene amine derivative, polyvinylpyrrolidone
		C−O stretching	polyoxyalkylene amine derivative, polyethylene glycol, ethylene glycol monobutyl ether
	v	C═C bending	nonylphenol
	vi	benzene derivative	nonylphenol
C@ pellet	vii	C−H stretching	OA
	viii	C═O stretching	
	ix	C−H bending	
	x	C−O stretching	
	xi	C═C bending	
D@ pellet	xii	C−H stretching	tetramethylammonium hydroxide (TMAOH)
	xiii	C−H bending	
	xiv	C−N stretching	
	xv	C−H bending	

[a]Nonylphenol, the polyoxyalkylene amine derivative, polyethylene glycol, polyvinylpyrrolidone, and ethylene glycol monobutyl ether.

nanoparticles and the surface functionalization of chemical groups, their hydrodynamic sizes are larger than the magnetic core sizes. For samples B@2k and D@2k, the hydrodynamic sizes of γ'-Fe_4N nanoparticles are very uniform with peaks at 44 and 41 nm, respectively. This proves that the commercial nanoparticle surfactants and TMAOH are good surface-active media for achieving the goal of extracting uniformly sized and sub-100 nm γ'-Fe_4N nanoparticles. On the other hand, from samples A@2k, A@11k, C@2k, and C@11k, severe clustering of γ'-Fe_4N nanoparticles is observed in TEM images and NTA results. Thus, water and OA do not appear to be good match for our purpose here. Furthermore, the FTIR results of these washed and dried γ'-Fe_4N nanoparticles indicate the successful surface functionalization of commercial surfactants (i.e., nonylphenol, the polyoxyalkylene amine derivative, polyethylene glycol, polyvinylpyrrolidone, and ethylene glycol monobutyl ether) and TMAOH. However, OA and water have failed in coating chemical groups on γ'-Fe_4N nanoparticles, which also explains the clustering and wider size distributions of nanoparticles from samples C@2k and C@11k.

Although this is a preliminary work on preparing ultrastable, monodispersed, uniformly sized, and sub-100 nm γ'-Fe_4N nanoparticle suspensions, this could open a new era of applying high-moment, inexpensive, environment-friendly, and low-biotoxicity MNPs in future biomedical applications. Future work will be the grafting of proteins (such as antibodies, protein molecules, peptides, enzymes, and so forth), nucleic acids (i.e., DNA and RNA), and drugs onto these surface-modified γ'-Fe_4N nanoparticles for *in vitro* and *in vivo* biomedical applications.

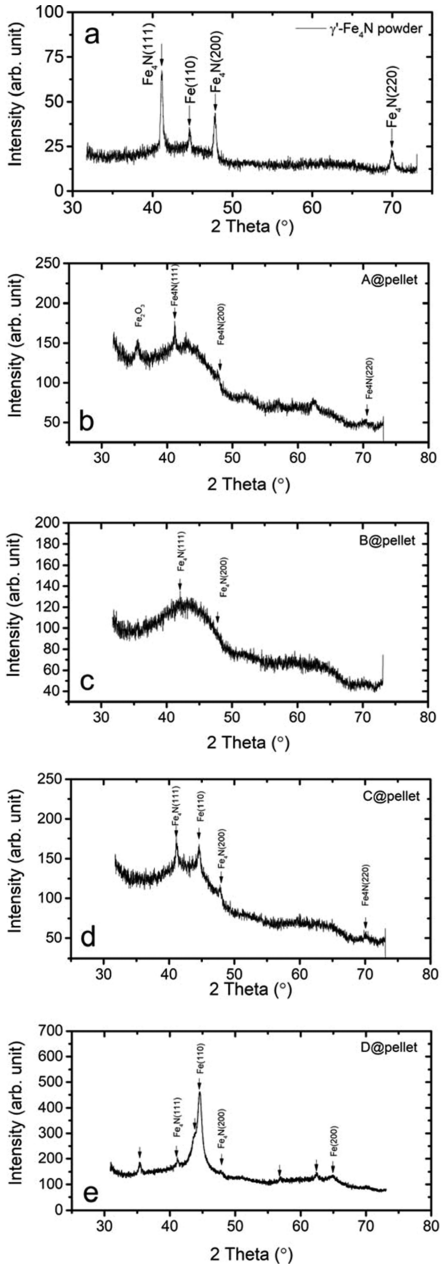

Figure 9. XRD patterns of (a) synthesized γ'-Fe_4N nanoparticle powder, (b) A@pellet, (c) B@pellet, (d) C@pellet, and (e) D@pellet; unlabeled arrows in (e) represent peaks caused by the iron oxide phase due to the partial oxidation of γ'-Fe_4N nanoparticles during XRD sample preparation and measurements.

■ ASSOCIATED CONTENT

Supporting Information

The Supporting Information is available free of charge at https://pubs.acs.org/doi/10.1021/acsanm.0c03421.

https://doi.org/10.1021/acsanm.0c03421
ACS Appl. Nano Mater. 2021, 4, 4409−4418

Photographs of γ'-Fe_4N nanoparticle colloidal suspensions; magnetic core size distributions of samples X@11k (X = A, B, and D) from TEM images; and hydrodynamic size distributions and percentile size distributions of samples X@11k (X = A, B, C, and D) (PDF)

AUTHOR INFORMATION

Corresponding Authors

Kai Wu − *Department of Electrical and Computer Engineering, University of Minnesota, Minneapolis, Minnesota 55455, United States;* orcid.org/0000-0002-9444-6112; Email: wuxx0803@umn.edu

Jian-Ping Wang − *Department of Electrical and Computer Engineering, University of Minnesota, Minneapolis, Minnesota 55455, United States;* Email: jpwang@umn.edu

Authors

Jinming Liu − *Department of Electrical and Computer Engineering, University of Minnesota, Minneapolis, Minnesota 55455, United States;* orcid.org/0000-0002-4313-5816

Renata Saha − *Department of Electrical and Computer Engineering, University of Minnesota, Minneapolis, Minnesota 55455, United States;* orcid.org/0000-0002-0389-0083

Bin Ma − *Department of Electrical and Computer Engineering, University of Minnesota, Minneapolis, Minnesota 55455, United States*

Diqing Su − *Department of Chemical Engineering and Material Science, University of Minnesota, Minneapolis, Minnesota 55455, United States;* orcid.org/0000-0002-5790-8744

Vinit Kumar Chugh − *Department of Electrical and Computer Engineering, University of Minnesota, Minneapolis, Minnesota 55455, United States*

Complete contact information is available at: https://pubs.acs.org/10.1021/acsanm.0c03421

Author Contributions

[§]K.W. and J.L. contributed equally to this work.

Notes

The authors declare no competing financial interest.

ACKNOWLEDGMENTS

This study was financially supported by the Institute of Engineering in Medicine of the University of Minnesota through the FY18 IEM Seed Grant Funding Program. This study was also financially supported by the U.S. Department of Agriculture-National Institute of Food and Agriculture (NIFA) under award no. 2020-67021-31956. Portions of this work were conducted in the Minnesota Nano Center, which is supported by the National Science Foundation through the National Nano Coordinated Infrastructure Network (NNCI) under award no. ECCS-1542202. Portions of this work were carried out in the Characterization Facility, University of Minnesota, a member of the NSF-Funded Materials Research Facilities Network (www.mrfn.org) via the MRSEC program.

REFERENCES

(1) Luo, Y.; Alocilja, E. C. Portable Nuclear Magnetic Resonance Biosensor and Assay for a Highly Sensitive and Rapid Detection of Foodborne Bacteria in Complex Matrices. *J. Biol. Eng.* **2017**, *11*, 14.

(2) Chen, K.-L.; Yeh, Y.-W.; Liao, S.-H.; Wu, C.-H.; Wang, L.-M. *Study of γ-Fe2O3/Au Core/Shell Nanoparticles as the Contrast Agent for High-T cSQUID-Based Low Field Nuclear Magnetic Resonance*; IEEE, 2016, pp 585−586.

(3) Hash, S.; Martinez-Viedma, M. P.; Fung, F.; Han, J. E.; Yang, P.; Wong, C.; Doraisamy, L.; Menon, S.; Lightner, D. Nuclear Magnetic Resonance Biosensor for Rapid Detection of Vibrio Parahaemolyticus. *Biomed. J.* **2019**, *42*, 187−192.

(4) Wu, K.; Su, D.; Saha, R.; Liu, J.; Wang, J.-P. Investigating the Effect of Magnetic Dipole−Dipole Interaction on Magnetic Particle Spectroscopy: Implications for Magnetic Nanoparticle-Based Bioassays and Magnetic Particle Imaging. *J. Phys. Appl. Phys.* **2019**, *52*, 335002.

(5) Graeser, M.; Thieben, F.; Szwargulski, P.; Werner, F.; Gdaniec, N.; Boberg, M.; Griese, F.; Möddel, M.; Ludewig, P.; van de Ven, D. Human-Sized Magnetic Particle Imaging for Brain Applications. *Nat. Commun.* **2019**, *10*, 1936.

(6) Moros, M.; Idiago-López, J.; Asín, L.; Moreno-Antolín, E.; Beola, L.; Grazú, V.; Fratila, R. M.; Gutiérrez, L.; de la Fuente, J. M. Triggering Antitumoural Drug Release and Gene Expression by Magnetic Hyperthermia. *Adv. Drug Deliv. Rev.* **2019**, *138*, 326−343.

(7) Hervault, A.; Dunn, A. E.; Lim, M.; Boyer, C.; Mott, D.; Maenosono, S.; Thanh, N. T. K. Doxorubicin Loaded Dual PH-and Thermo-Responsive Magnetic Nanocarrier for Combined Magnetic Hyperthermia and Targeted Controlled Drug Delivery Applications. *Nanoscale* **2016**, *8*, 12152−12161.

(8) Blanco-Andujar, C.; Teran, F.; Ortega, D. Current Outlook and Perspectives on Nanoparticle-Mediated Magnetic Hyperthermia. *Iron Oxide Nanoparticles for Biomedical Applications*; Elsevier, 2018, pp 197−245.

(9) Soleymani, M.; Velashjerdi, M.; Shaterabadi, Z.; Barati, A. One-Pot Preparation of Hyaluronic Acid-coated Iron Oxide Nanoparticles for Magnetic Hyperthermia Therapy and Targeting CD44-Overexpressing Cancer Cells. *Carbohydr. Polym.* **2020**, *237*, 116130.

(10) Hedayatnasab, Z.; Dabbagh, A.; Abnisa, F.; Daud, W. M. A. W. Polycaprolactone-Coated Superparamagnetic Iron Oxide Nanoparticles for In Vitro Magnetic Hyperthermia Therapy of Cancer. *Eur. Polym. J.* **2020**, *133*, 109789.

(11) Wu, K.; Su, D.; Liu, J.; Saha, R.; Wang, J.-P. Magnetic Nanoparticles in Nanomedicine: A Review of Recent Advances. *Nanotechnology* **2019**, *30*, 502003.

(12) Wu, K.; Su, D.; Saha, R.; Liu, J.; Chugh, V. K.; Wang, J.-P. Magnetic Particle Spectroscopy: A Short Review of Applications Using Magnetic Nanoparticles. *ACS Appl. Nano Mater.* **2020**, *3*, 4972−4989.

(13) Klein, T.; Wang, W.; Yu, L.; Wu, K.; Boylan, K. L. M.; Vogel, R. I.; Skubitz, A. P. N.; Wang, J.-P. Development of a Multiplexed Giant Magnetoresistive Biosensor Array Prototype to Quantify Ovarian Cancer Biomarkers. *Biosens. Bioelectron.* **2019**, *126*, 301−307.

(14) Wu, K.; Chugh, V. K.; Di Girolamo, A.; Liu, J.; Saha, R.; Su, D.; Krishna, V. D.; Nair, A.; Davies, W.; Wang, Y. A.; Cheeran, M. C.-J.; Wang, J.-P. A Portable Magnetic Particle Spectrometer for Future Rapid and Wash-Free Bioassays. *ACS Appl. Mater. Interfaces* **2021**, *13*, 7966−7976.

(15) Denmark, D. J.; Bustos-Perez, X.; Swain, A.; Phan, M.-H.; Mohapatra, S.; Mohapatra, S. S. Readiness of Magnetic Nanobiosensors for Point-of-Care Commercialization. *J. Electron. Mater.* **2019**, *48*, 4749−4761.

(16) Ferreira, M.; Sousa, J.; Pais, A.; Vitorino, C. The Role of Magnetic Nanoparticles in Cancer Nanotheranostics. *Materials* **2020**, *13*, 266.

(17) Malhotra, N.; Lee, J.-S.; Liman, R. A. D.; Ruallo, J. M. S.; Villaflores, O. B.; Ger, T.-R.; Hsiao, C.-D. Potential Toxicity of Iron Oxide Magnetic Nanoparticles: A Review. *Molecules* **2020**, *25*, 3159.

(18) Hettiarachchi, M. A.; Abdelhamid, E.; Nadgorny, B.; Brock, S. L. Anisotropic Manganese Antimonide Nanoparticle Formation by Solution−Solid−Solid Growth Mechanism: Consequence of Sodium Borohydride Addition towards Reduced Surface Oxidation and Enhanced Magnetic Moment. *Nanoscale* **2019**, *11*, 6886−6896.
(19) Wu, K.; Liu, J.; Saha, R.; Ma, B.; Su, D.; Peng, C.; Sun, J.; Wang, J.-P. Irregularly Shaped Iron Nitride Nanoparticles as a Potential Candidate for Biomedical Applications: From Synthesis to Characterization. *ACS Omega* **2020**, *5*, 11756−11767.
(20) Wu, X. L.; Zhong, W.; Jiang, H. Y.; Tang, N. J.; Zou, W. Q.; Du, Y. W. Magnetic Properties and Thermal Stability of Γ′-Fe4N Nanoparticles Prepared by a Combined Method of Reduction and Nitriding. *J. Magn. Magn. Mater.* **2004**, *281*, 77−81.
(21) Dhanasekaran, P.; Salunke, H. G.; Gupta, N. M. Visible-Light-Induced Photosplitting of Water over Γ′-Fe4N and Γ′-Fe4N/α-Fe2O3 Nanocatalysts. *J. Phys. Chem. C* **2012**, *116*, 12156−12164.
(22) Zhang, C.; Liu, X.; Li, M.; Liu, C.; Li, H.; Meng, X.; Rehman, K. M. U. Preparation and Soft Magnetic Properties of Γ′-Fe4N Particles. *J. Mater. Sci. Mater. Electron.* **2018**, *29*, 1254−1257.
(23) Peng, X.; Yu, S.; Chang, J.; Ge, M.; Li, J.; Ellis, T.; Yang, Y.; Xu, J.; Hong, B.; Jin, D.; Jin, H.; Wang, X.; Ge, H. Preparation and Magnetic Properties of Fe4N/Fe Soft Magnetic Composites Fabricated by Gas Nitridation. *J. Magn. Magn. Mater.* **2020**, *500*, 166407.
(24) Tran, N.; Webster, T. J. Magnetic Nanoparticles: Biomedical Applications and Challenges. *J. Mater. Chem.* **2010**, *20*, 8760−8767.
(25) Yang, H. Y.; Li, Y.; Lee, D. S. Multifunctional and Stimuli-responsive Magnetic Nanoparticle-based Delivery Systems for Biomedical Applications. *Adv. Ther.* **2018**, *1*, 1800011.
(26) Cardoso, V. F.; Francesko, A.; Ribeiro, C.; Bañobre-López, M.; Martins, P.; Lanceros-Mendez, S. Advances in Magnetic Nanoparticles for Biomedical Applications. *Adv. Healthcare Mater.* **2018**, *7*, 1700845.
(27) Mohammed, L.; Gomaa, H. G.; Ragab, D.; Zhu, J. Magnetic Nanoparticles for Environmental and Biomedical Applications: A Review. *Particuology* **2017**, *30*, 1−14.
(28) Elrefai, A. L.; Yoshida, T.; Enpuku, K. Magnetic Parameters Evaluation of Magnetic Nanoparticles for Use in Biomedical Applications. *J. Magn. Magn. Mater.* **2019**, *474*, 522−527.
(29) Noorizadeh, H.; Farmany, A. Adsorptive Removal of Arsenic from Aqueous Solutions Using Amino Functionalized Super Paramagnetic Iron Oxide Nanoparticle/SiO2. *Adv. J. Chem., Sect. A* **2019**, *2*, 128−135.
(30) Ansari, S.; Ficiarà, E.; Ruffinatti, F.; Stura, I.; Argenziano, M.; Abollino, O.; Cavalli, R.; Guiot, C.; D'Agata, F. Magnetic Iron Oxide Nanoparticles: Synthesis, Characterization and Functionalization for Biomedical Applications in the Central Nervous System. *Materials* **2019**, *12*, 465.
(31) Aisida, S. O.; Akpa, P. A.; Ahmad, I.; Zhao, T.-k.; Maaza, M.; Ezema, F. I. Bio-Inspired Encapsulation and Functionalization of Iron Oxide Nanoparticles for Biomedical Applications. *Eur. Polym. J.* **2020**, *122*, 109371.
(32) Nosrati, H.; Salehiabar, M.; Davaran, S.; Ramazani, A.; Manjili, H. K.; Danafar, H. New Advances Strategies for Surface Functionalization of Iron Oxide Magnetic Nano Particles (IONPs). *Res. Chem. Intermed.* **2017**, *43*, 7423−7442.
(33) Hufschmid, R.; Teeman, E.; Mehdi, B. L.; Krishnan, K. M.; Browning, N. D. Observing the Colloidal Stability of Iron Oxide Nanoparticles in Situ. *Nanoscale* **2019**, *11*, 13098−13107.
(34) Wulandari, I. O.; Sulistyarti, H.; Safitri, A.; Santjojo, D. J. H.; Sabarudin, A. Development of Synthesis Method of Magnetic Nanoparticles Modified by Oleic Acid and Chitosan as a Candidate for Drug Delivery Agent. *Development* **2019**, *9*, 1.
(35) Patil, R. M.; Shete, P. B.; Thorat, N. D.; Otari, S. V.; Barick, K. C.; Prasad, A.; Ningthoujam, R. S.; Tiwale, B. M.; Pawar, S. H. Non-Aqueous to Aqueous Phase Transfer of Oleic Acid Coated Iron Oxide Nanoparticles for Hyperthermia Application. *RSC Adv.* **2014**, *4*, 4515−4522.
(36) Lai, C. W.; Low, F. W.; Tai, M. F.; Abdul Hamid, S. B. Iron Oxide Nanoparticles Decorated Oleic Acid for High Colloidal Stability. *Adv. Polym. Technol.* **2018**, *37*, 1712−1721.
(37) Moya, C.; Batlle, X.; Labarta, A. The Effect of Oleic Acid on the Synthesis of Fe 3−x O 4 Nanoparticles over a Wide Size Range. *Phys. Chem. Chem. Phys.* **2015**, *17*, 27373−27379.
(38) Korpany, K. V.; Majewski, D. D.; Chiu, C. T.; Cross, S. N.; Blum, A. S. Iron Oxide Surface Chemistry: Effect of Chemical Structure on Binding in Benzoic Acid and Catechol Derivatives. *Langmuir* **2017**, *33*, 3000−3013.
(39) Amstad, E.; Gillich, T.; Bilecka, I.; Textor, M.; Reimhult, E. Ultrastable Iron Oxide Nanoparticle Colloidal Suspensions Using Dispersants with Catechol-Derived Anchor Groups. *Nano Lett.* **2009**, *9*, 4042−4048.
(40) Sharifi Dehsari, H.; Harris, R. A.; Ribeiro, A. H.; Tremel, W.; Asadi, K. Optimizing the Binding Energy of the Surfactant to Iron Oxide Yields Truly Monodisperse Nanoparticles. *Langmuir* **2018**, *34*, 6582−6590.
(41) Andrade, Â. L.; Valente, M. A.; Ferreira, J. M. F.; Fabris, J. D. Preparation of Size-Controlled Nanoparticles of Magnetite. *J. Magn. Magn. Mater.* **2012**, *324*, 1753−1757.
(42) Andrade, Â. L.; Fabris, J. D.; Ardisson, J. D.; Valente, M. A.; Ferreira, J. M. Effect of Tetramethylammonium Hydroxide on Nucleation, Surface Modification and Growth of Magnetic Nanoparticles. *J. Nanomater.* **2012**, *2012*, 1.
(43) Zulhijah, R.; Nandiyanto, A. B. D.; Ogi, T.; Iwaki, T.; Nakamura, K.; Okuyama, K. Effect of Oxidation on α″-Fe16N2 Phase Formation from Plasma-Synthesized Spherical Core−Shell α-Fe/Al2O3 Nanoparticles. *J. Magn. Magn. Mater.* **2015**, *381*, 89−98.
(44) Liu, J.; Guo, G.; Zhang, F.; Wu, Y.; Ma, B.; Wang, J.-P. Synthesis of A″-Fe 16 N 2 Ribbons with a Porous Structure. *Nanoscale Adv.* **2019**, *1*, 1337−1342.
(45) Liu, J.; Guo, G.; Zhang, X.; Zhang, F.; Ma, B.; Wang, J.-P. Synthesis of α ″-Fe16N2 Foils with an Ultralow Temperature Coefficient of Coercivity for Rare-Earth-Free Magnets. *Acta Mater.* **2020**, *184*, 143−150.
(46) Ma, B.; Liu, J.; Guo, G.; Wang, J.-P. Critical Thickness of α ″-Fe16N2 Layer Prepared in Low-Temperature Nitriding. *J. Appl. Phys.* **2020**, *128*, 223902.
(47) Ito, K.; Rougemaille, N.; Pizzini, S.; Honda, S.; Ota, N.; Suemasu, T.; Fruchart, O. Magnetic Domain Walls in Nanostrips of Single-Crystalline Fe4N (001) Thin Films with Fourfold in-Plane Magnetic Anisotropy. *J. Appl. Phys.* **2017**, *121*, 243904.
(48) Costa-Krämer, J. L.; Borsa, D. M.; García-Martín, J. M.; Martín-González, M. S.; Boerma, D. O.; Briones, F. Structure and Magnetism of Single-Phase Epitaxial Γ′− Fe 4 N. *Phys. Rev. B: Condens. Matter Mater. Phys.* **2004**, *69*, 144402.
(49) Kendelewicz, T.; Kaya, S.; Newberg, J. T.; Bluhm, H.; Mulakaluri, N.; Moritz, W.; Scheffler, M.; Nilsson, A.; Pentcheva, R.; Brown, G. E., Jr. X-Ray Photoemission and Density Functional Theory Study of the Interaction of Water Vapor with the Fe3O4 (001) Surface at near-Ambient Conditions. *J. Phys. Chem. C* **2013**, *117*, 2719−2733.
(50) Yamamoto, S.; Kendelewicz, T.; Newberg, J. T.; Ketteler, G.; Starr, D. E.; Mysak, E. R.; Andersson, K. J.; Ogasawara, H.; Bluhm, H.; Salmeron, M.; Brown, G. E.; Nilsson, A. Water Adsorption on α-Fe2O3 (0001) at near Ambient Conditions. *J. Phys. Chem. C* **2010**, *114*, 2256−2266.
(51) Van Voorthuysen, E. D. M.; Boerma, D. O.; Chechenin, N. C. Low-Temperature Extension of the Lehrer Diagram and the Iron-Nitrogen Phase Diagram. *Metall. Mater. Trans. A* **2002**, *33*, 2593−2598.
(52) Wang, Y.; Li, Y.; Rong, C.; Liu, J. P. Sm−Co Hard Magnetic Nanoparticles Prepared by Surfactant-Assisted Ball Milling. *Nanotechnology* **2007**, *18*, 465701.

https://doi.org/10.1021/acsanm.0c03421
ACS Appl. Nano Mater. 2021, 4, 4409−4418